Graphene nanoarchitectures: production and characterization

OTKA K101599 (2012 - 2016)

Principal Investigator: Prof. Dr. László P. Biró, corresponding member of the Hungarian Academy of Sciences

The list below briefly outlines the main groups of achievements, with the associated publications. The ordering of the topics is not in a time sequence, but more in a logical hierarchy and terminates with a number of reviews - some of them written as invited papers – which present the status of a certain segment of the field at a given moment. The numbers in square brackets correspond with the numbers in the list of publications belonging to this final report.

1. Atomic scale modelling of the charge propagation in graphene [1, 14, 43, 50]
   - Waveguides in graphene with grain boundaries [2]
   - Effects of detects [3, 17, 18, 52]

2. Methods for the characterization of the CVD graphene
   - Polarized light microscopy [4, 7]
   - Structural and electronic properties of individual grain boundaries [5, 8, 11, 12, 21, 22, 27, 30, 37]
   - Computer modeling of grain boundaries [13, 21, 22, 25, 28, 29, 30, 31, 44, 45]

3. Atomic scale nanoengineering
   - Selective etching of armchair edges in graphene [16]
   - Scanning probe microscopy characterization and nanopatterning of CVD graphene [19, 35, 36, 39, 40]
   - Armchair and zig-zag edge nanoribbons [26, 34, 38, 41, 42, 53, 54, 55]

4. Sub-nanometer rippling of CVD graphene on Cu(111) [6, 23, 24]

5. Vertical wan der Waals heterostructures of 2D materials
   CVD graphene grown on h-BN [10]
   Graphene on HOPG [49, 66]
   Exfoliation of other 2D materials [51, 65]
   MoS_2 grown on HOPG [58, 59, 60]

6. 3D heteronanoarchitectures with graphene [32, 33, 46, 47, 48, 56, 57, 61, 62, 63, 68, 69]

7. REVIEWS
   Graphene: nanoscale processing and recent applications [9]
   Atomi vastagságú anyagok, MTA székfoglaló előadás, 2013 [15]
   Grain boundaries in graphene grown by chemical vapor deposition [20]
   Wave packet dynamical calculations for carbon nanostructures [64]
   Grain boundaries in chemical vapor deposition-grown graphene [67]

Short history

The proposal of the present project was submitted while the Research Institute for Technical Physics and Materials Science (MFA) of the Hungarian Academy of Sciences (HAS) was an autonomous institute (2011). The carrying out of the proposed work started when the MFA was already integrated in the Research Centre for Natural Sciences of the HAS (2012), and was finished when the MFA was not any more integrated in the Research Centre for Natural Sciences, but it was integrated in the Centre for Energy Research of the HAS (2016). These changes affected the carrying out of the planned work under several aspects, including that of the flow of funding from the funding body to the research centre, to which MFA was belonging at a given moment, and the way in which the researchers could use those resources. This is the reason of extending the planned project duration by one year.

1. Atomic scale modelling of the charge propagation in graphene [1, 14, 43, 50]

Graphene is different from the semiconductor materials commonly used in microelectronics because it has a linear energy dispersion relation near the Fermi level. The $E(k_x, k_y)$ function is shaped like an inverted pair of cones that meet in a single point — the so-called Dirac point — in momentum space. This photon-like, quasirelativistic behavior gives rise to a variety of phenomena which was not possible to study in condensed matter physics, such as the Klein paradox, Andreev reflection, Veselago lens, etc. This $E \approx E_F$ (near-to-Fermi-energy) behavior of graphene band structure has been extensively studied in recent years theoretically and also experimentally. Because of the high mobility and long coherence length, the details of many-body interactions and strong coherence over reasonable sizes means that the simple quasiclassical approaches used in most semiconductor devices are not adequate in graphene. Less is known, however, about the high excitation energy range when $E - E_F > 1$ eV (i.e., about the far-from-Fermi-energy domain). It was shown that electron beam splitting, collimation, and beam guiding can all be realized by heterodimensional graphene junctions, without applying an external electric field. This is possible in the hot-energy region, where the $E(\mathbf{k})$ dispersion relation, which is isotropic near the Fermi energy [i.e. $E(\mathbf{k}) = E(k)$ if $k \approx k_F$] becomes anisotropic if k is far from k_F .

Scanning tunneling microscopy (STM) is one of the main techniques used to investigate with atomic resolution carbon nanostructures and devices fabricated from them. Therefore the precise understanding of the STM imaging mechanism(i.e., the current flow from the STM tip to the graphene surface) is important for nanotechnology. An atomically sharp STM tip is a quantum tunneling contact (QTC). Similarly to a quantum point contact (QPC), the electrons can enter from the tip into the sample only through a narrow channel (its width is 0.1–0.2 nm for atomically sharp tips), but contrary to a QPC, no conducting channel exists; electrons can cross the channel only via the tunnel effect. The charge transfer through a QTC is different from that of a QPC both quantitatively and qualitatively. The tunneling probability in an STM experiment is typically $T = 10^{-6}$–10^{-3}, hence the resistance of an STM QTC is several MΩ instead of the $h/2e^2$ =13 kΩ minimal value characteristic of a QPC. The few electrons that tunnel are selected so that the transverse momentum and the higher-energy electrons are preferred by the QTC. Moreover, when the STM sample is not a simple metal, the tunneling process includes complicated multiple scattering and interference effects between the tip states and sample states. The outcome of this complex scattering process determines $T(\mathbf{k})$, the transmission probability as the function of the incoming momentum. Only those few electrons surviving this selection process remain on the sample and can spread on it, reaching the other (ground) STM electrode after a macroscopic spreading. The pattern of this eventual spreading is determined by two factors: i) the band structure of the sample and ii) the pattern of

electronic waves remaining on the sample at the end of the initial selection process mentioned above. One can distinguish two spatial regions in an STM tip–sample system: the near and far regions, somewhat similar to the near- and far-field regions distinguished for a radiating electromagnetic antenna. The region that participates at the multiple scattering process between tip and sample is the near region. That region where the influence of the tip is negligible is the far region.

We examined in detail the dynamics of the STM tunneling process from an atomically sharp STM tip onto the graphene surface, both in the near and the far regions. The analysis is performed both in time and energy domain, giving a full picture of the quasiparticle dynamics within the level of the local one-electron pseudopotential model of graphene. In order to reduce the many-particle problem into a one-particle problem we used a local one-electron pseudopotential matching the ab initio band structure of graphene as well as possible. In our calculation a Gaussian wave packet (WP) is injected into the graphene sheet from the simulated metallic STM tip and its time development is calculated by wave packet dynamics.

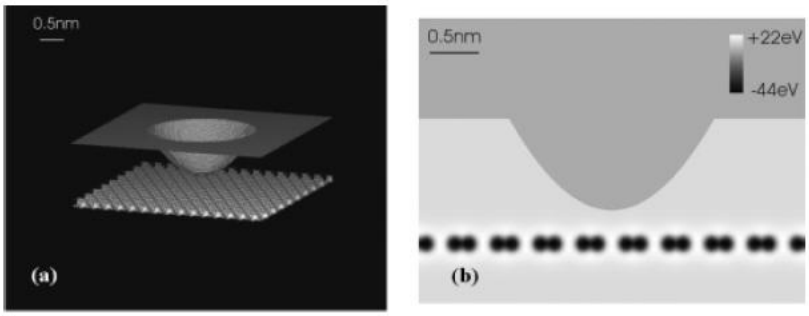

FIG. 1. Model geometry of the STM tip graphene system. (a) −2.7 eV equipotential surface of the potential. The surface is clipped at the boundary of the presentation box. (b) Grayscale image of the 2D cross section of the potential. The hyperbolic protrusion on the upper half plane and the horizontal row of black dots represent the vertical cross sections of the tip and graphene, respectively. Black (white) denotes smallest (largest) potential values. The dark gray level at the upper part is the negative potential inside the STM tip (−9.81 eV), the light gray level at the lower part is the vacuum potential (zero).

The use of the above detailed computer simulation method allowed us to investigate in detail the charge transfer process between the STM tip and the graphene sheet. There are two distinct regions: the region in the vicinity of the tunneling point (the position of the STM tip), where the spreading of the tunneled charge is dominated by molecular-type processes and a region at a larger distance, where the tunneling charge has "sampled" a large enough area for the solid state-type processes to take over. In order to understand this peculiar anisotropic spreading around E_F, we performed a detailed investigation of the dynamics of the transient period, which begins when the WP tunnels from the STM tip onto the graphene surface and lasts until the stable, far region spreading pattern is formed. As the WP reaches the tip apex from inside the tip bulk, it begins to tunnel onto the central hexagon (i.e., that below the tip apex, t = 1.22 fs). Then the wave packet begins to spread on the graphene sheet along the C-C bonds, following the hexagonal symmetry (t = 2.00 fs, t = 2.45 fs). At t = 3.14 fs, after spreading 1.2 nm from the center, the direction of the spreading is changed. Further spreading (t = 3.52 fs, 4.19 fs) occurs along the 6 ΓK directions of the Brillouin zone, which matches the zigzag direction of the graphene sheet in direct space. This is illustrated in Fig. 2.

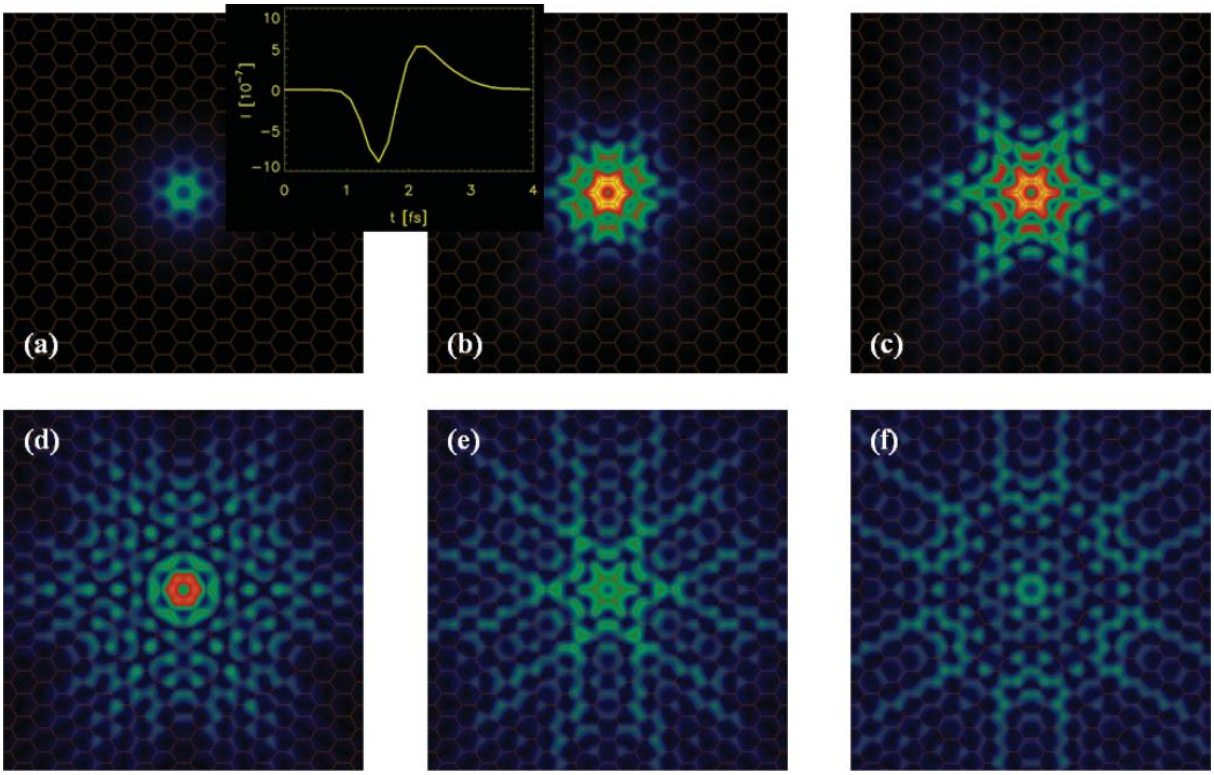

FIG. 2. Selected snapshots from the time evolution of the probability density of wave packet shown as color-coded 2D sections. Black corresponds to zero probability. We used the same color scale on all images, determined by the maximum probability density on the graphene sheet. The graphene network is shown by thin orange lines. Time values are: 1.22 fs, 2.00 fs, 2.45 fs, 3.14 fs, 3.52 fs, 4.19 fs. Size of the presentation window is 3.84 nm in both x and y directions. The inset shows the probability current I(t) flowing from the tip into the graphene surface.

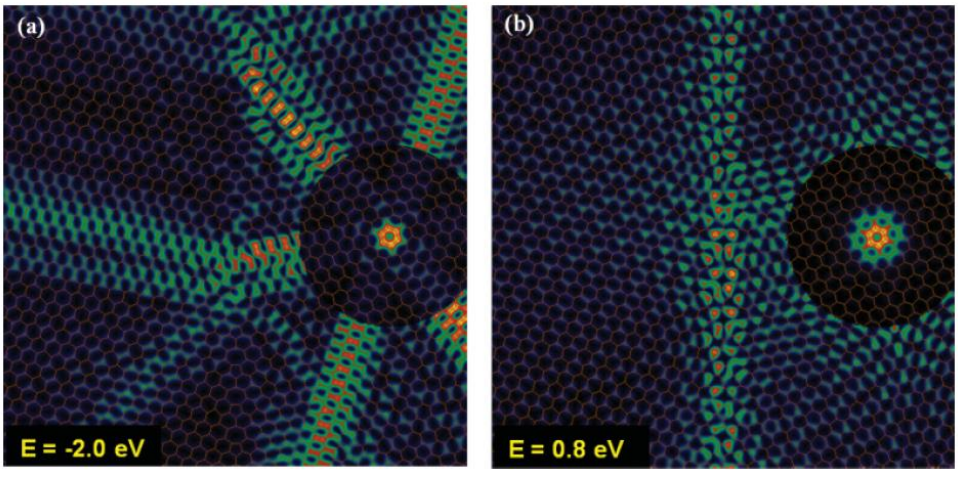

FIG. 3. Probability density on the graphene sheet with the grain boundary for selected energies shown as color-coded 2D sections. Black corresponds to zero density, bright yellow to the maximum density. The far region is shown on a separate (enhanced) color scale. The graphene network is shown by thin orange lines. Size of the presentation window is 7.68 nm.

The same approach allowed us to investigate the effects of defects, including extended defects, like grain boundaries (GB). These may have a strong perturbation on the charge propagation phenomena as illustrated in Fig. 3. The way in which the GBs affect charge propagation is energy dependent. These computer simulations constituted the clue in a later phase of our work, when we elucidated the processes occurring in the STM characterization of the GBs. WE also showed that two such grain boundaries if parallel to each other and plced close to each other may act as wave-guide.

2. Methods for the characterization of the CVD graphene

We dedicated important efforts in the direction of the characterization of the graphene sheets produced by chemical vapor deposition (CVD). If future practical applications of the graphene nanoelectronics is envisaged this step is unavoidable. We combined the full range of our experimental and modelling procedures to get more insight in the structure and the electronic properties of the grain boundaries.

We developed a fast optical method based on the coupling of the polarized light in propagating modes inside de graphene sheet, which allowed us to quickly identify the grains of CVD graphene grown on polycrystalline Cu and which also gives information on the orientation of the Cu grains on which the growth took place, Fig. 4.

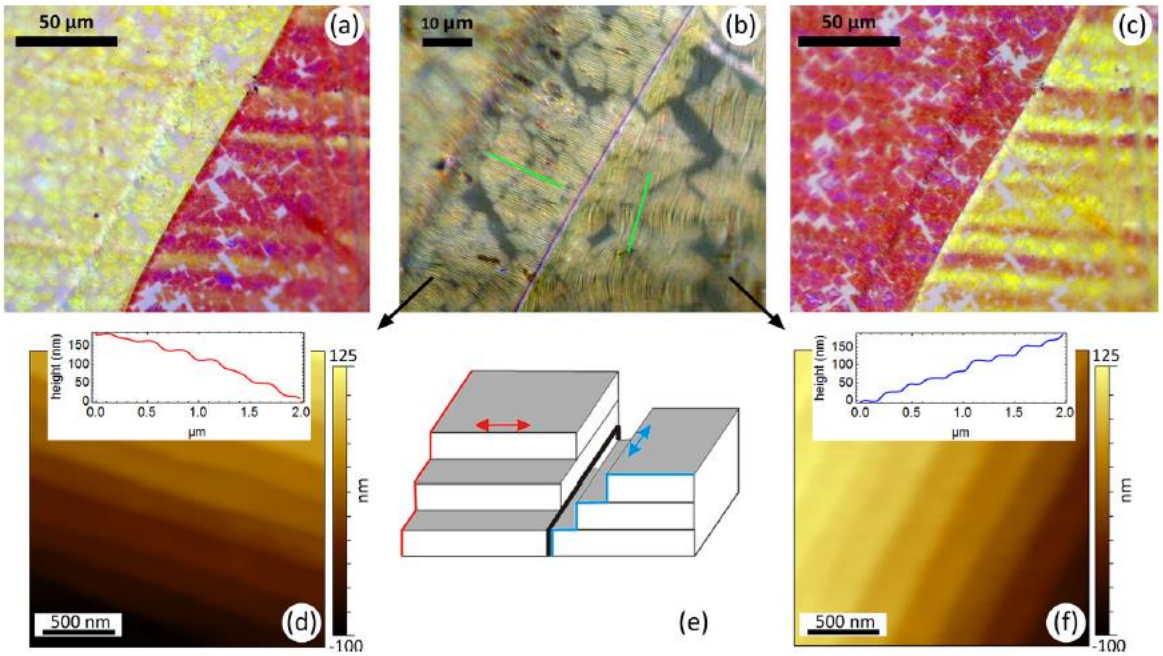

Fig. 4. Neighboring Cu grains with yellow/violet coloration and their characteristic step structure as revealed by polarized light microscopy (PM) and AFM images. (a), (c) yellow/violet and violet/yellow coloration at $(90+\Delta^{o})$ and $(90-\Delta^{o})$ setting of the analyzer; (b) high resolution PM image with rigorously crossed polarizer and analyzer. Note the parallel steps in each grain. The green lines indicate the average step edge direction; (d), (f) contact mode AFM image of the two grains; (e) schematic presentations of the step structure in the two grains, the shaded faces are roughly parallel with the surface of the Cu foil.

For the atomic scale characterization of the misorientation of neighboring graphene grain in CVD graphene we developed both AFM and STM based methods. While the AFM based

methods are more handy and faster the STM based methods also allow the characterization of the electronic properties of the grain boundaries.

We showed that a mild oxidation of the CVD graphene attacks selectively the GB regions, making possible in this way the mapping of the grain structure, and if lattice resolution AFM images are acquired the misorientation of the neighboring grain scan be also investigated. Fig. 5.

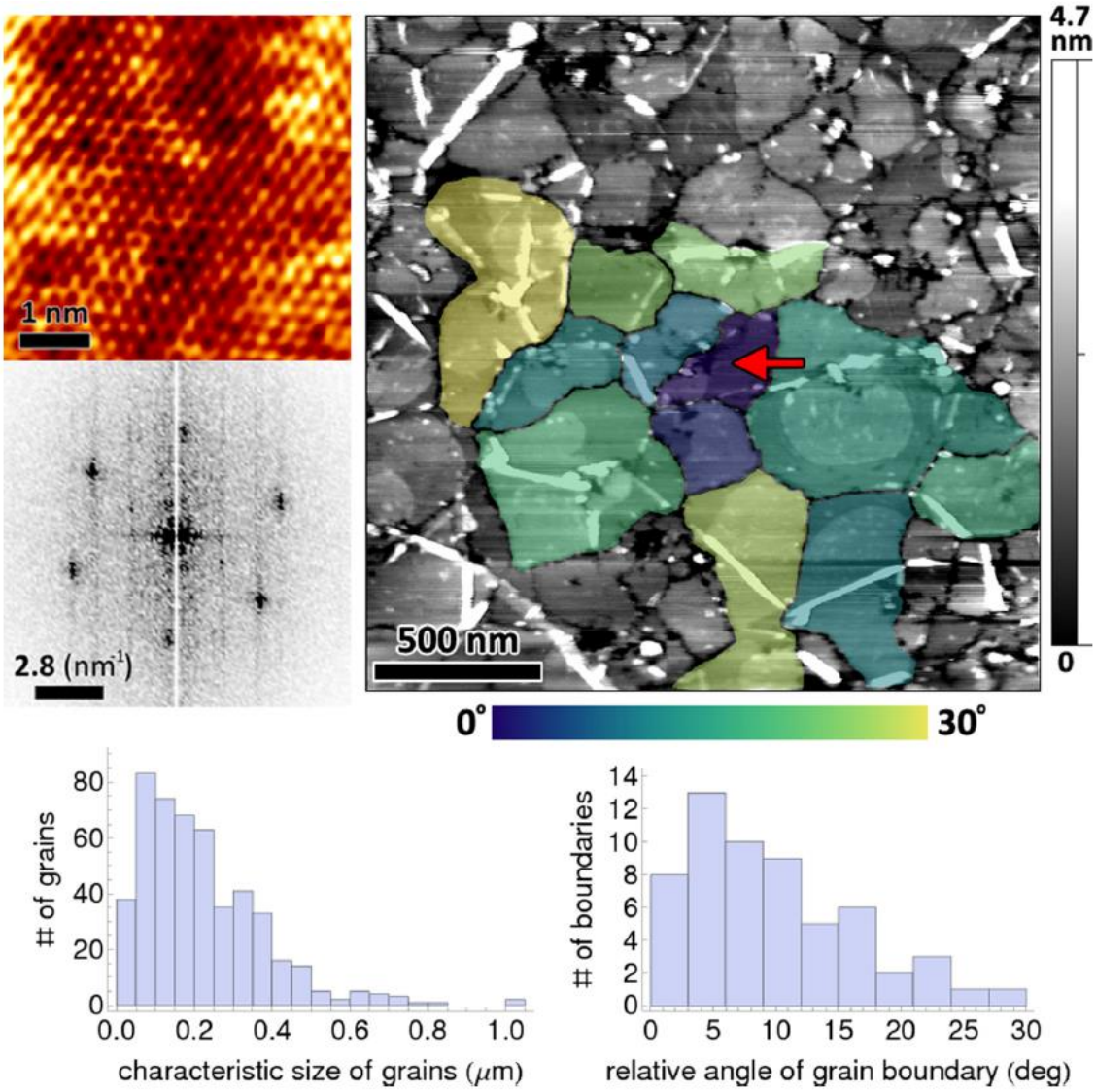

FIG. 5. AFM image of CVD graphene showing the etch trenches. By comparing the Fourier transform of atomic resolution AFM images of individual grains, one can make a false color map of the crystallographic orientation of the grains relative to a given direction. Two small images to the left show one such atomic resolution image and the Fourier transform thereof. The atomic resolution image was recorded by contact mode AFM on the grain shown by the red arrow. Histograms at the bottom show the distribution of the grain size (left) and the relative angle of the grains forming the boundaries (right). This data is a compilation of multiple AFM mapping measurements.

Despite the fact that the STM cannot reveal the precise atomic position of the C atoms where the crystalline lattices of the two neighboring grains with different orientations meet each other – like it is possible to be done with aberration corrected TEM – the STM has the major advantage that it is able to characterize the local electronic properties of the GB itself, Fig. 6.

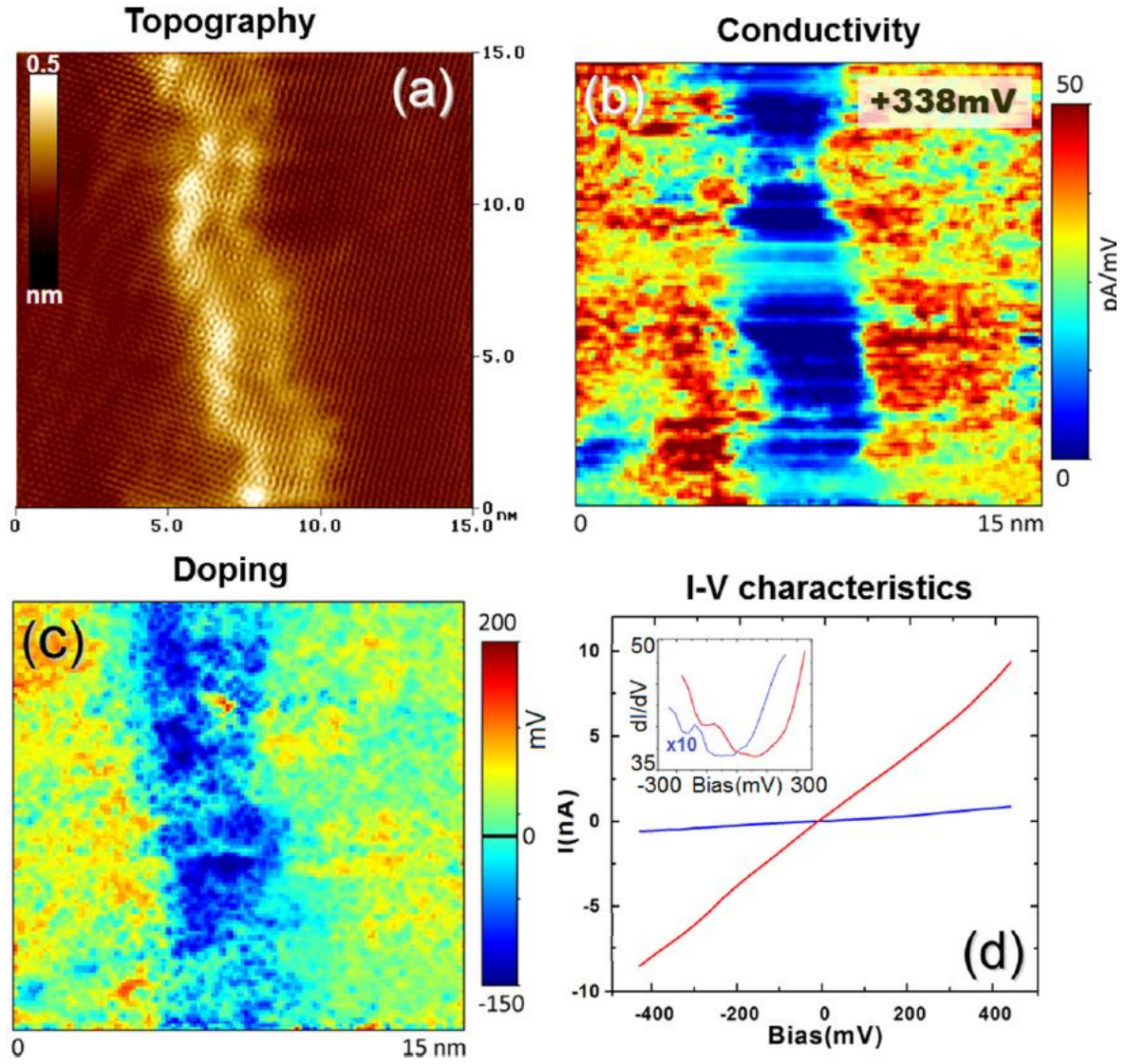

FIG. 6. (a) Atomic resolution constant current topographic STM image (100 mV, 1 nA) of a 29^{o} graphene grain boundary, with the boundary region displaying a bright contrast. (b) Spatially resolved tunneling conductivity map revealing a markedly suppressed conductivity at the grain boundary region. (c) Spatial map of the Dirac point position relative to the Fermi energy, indicating the local doping. (d) Representative individual current-voltage characteristics acquired at the grain boundary (low, blue) and over the unperturbed graphene lattice (steep, red). The corresponding numerical derivatives (differential conductance) are shown in the inset.

The careful evaluation of statistically relevant numbers of scanning tunneling spectroscopy (STS) spectra acquired over graphene GBs allowed to identify the general features of such grain boundaries. While far from the GB, the graphene did not revealed any unusual spectral features, three characteristic features were found when averaging more than 60 spectra

acquired over GBs: a maximum in the range of -0.4 eV, a maximum slightly above 0 eV – this one being the strongest one – and third maximum in the range of 0. 4 eV, Fig. 7. According to literature, the maxima at -0.4 eV and at 0.4 eV are associated with regular grain boundaries constructed of pentagons and heptagons (5-7 GB).

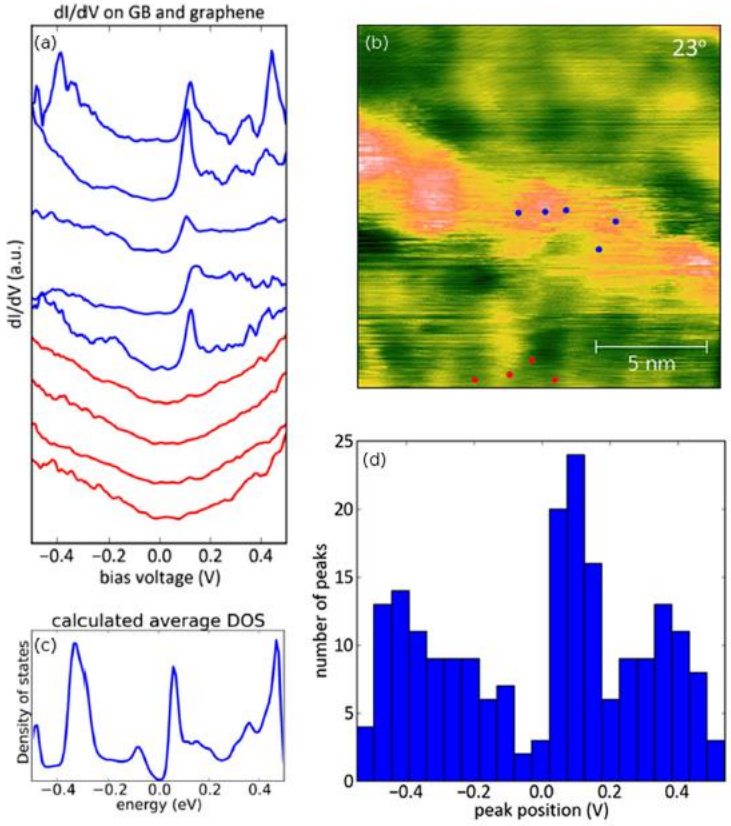

FIG. 7 – (a) dI/dV plots measured at selected points shown on the topography image. (b) Blue curves were measured on the GB and red curves on the graphene, the positions of the measurement are shown by similarly colored dots. (c) statistical average of the density of states of the six disordered GBs, calculated by DFT. (d) Histogram of the positions of LDOS peaks in 60 dI/dV spectra, measured over different positions on three distinct GBs (misorientation angles: 23^o, 25.5^o, 27^o).

By calculating the Density of States (DOS) of the different defected GB structures originating from the regular 5-7GB, by removing individual C atoms and relaxing the structure, it was possible to show that the most intense, previously unassigned maximum in Fig. 7d is associated with the GBs containing C vacancies. We call these GBs disordered GBs. The construction and the structure of such model GBs is shown in Fig. 8.

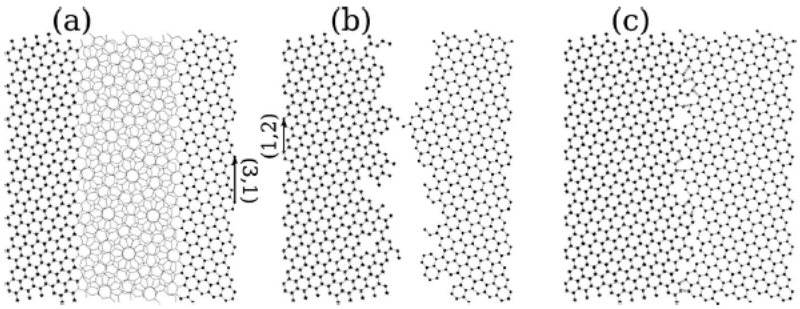

FIG. 8 – Construction of a disordered grain boundary between two graphene cells oriented such that their translation vectors (1,2) (left-hand side grain) and (3,1) (right-hand side grain) are parallel to one another. Occupied sites are represented by star symbols (left-hand side lattice) and filled circles (right-hand side lattice). The lattices of the cells overlap over a region where all the atoms have been removed (moire´ pattern in panel (a)). In panel (b), 250 atoms have been added in the transition region, following the algorithm given in the text. In panel (c), the transition region has been filled in with 401 atoms. Possible bonds between the two grains, before any structural relaxation, are shown by thick dashed lines. The final structure is determined by geometry optimization.

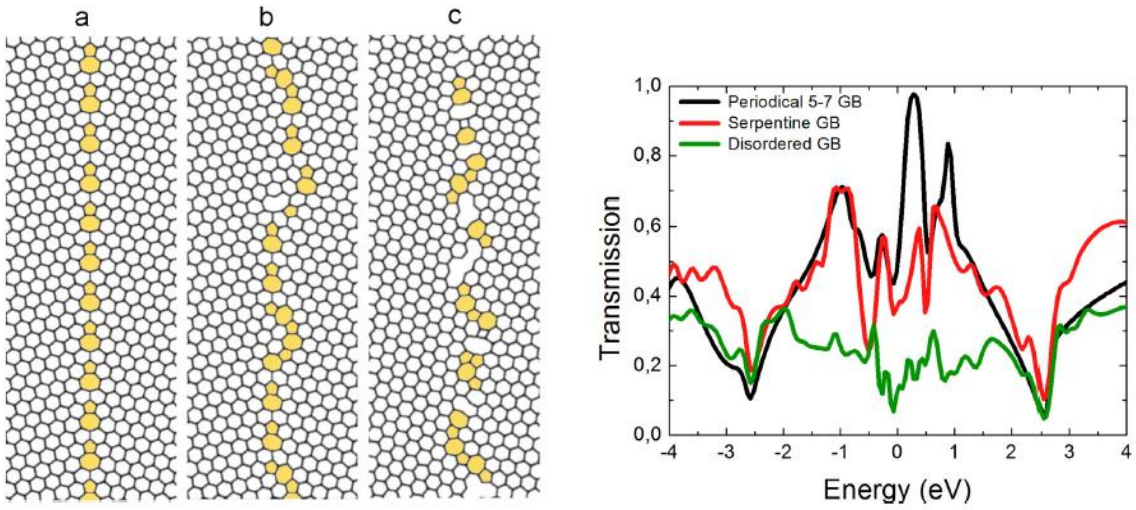

FIG. 9. Structures of the GBs, pentagons and heptagons are highlighted. (a) Periodical pentagon–heptagon GB. (b) Serpentine GB without periodicity. (c) Disordered GB containing several defects and non-hexagonal carbon rings. Structure (b) and (c) generated by a Monte-Carlo like procedure. Right hand panel: transmission functions of the GBs in (a), (b) and (c). The similar energy positions of the peak sin the case of the periodical 5–7 (black line) and serpentine GB (red line) originated from the pentagons and heptagons. Reduced transmission values appear for the low energy charge carriers in the case of the disordered GB (green line).

Using the WPD technique, presented in Section 1. we were able to compute the transmission through the tree typical grain boundaries shown in Fig. 9. In agreement with our own experimental data and data published in the literature the disordered Gb has the lowest transmission. As discussed in our reviews written on the topic of GBs in CVD graphene, the character of the GB formed between two growing together graphene grains is decided to a great extent by their lattice misorientation. Therefore this is the parameter that has to be controlled to achieve good quality CVD graphene.

3. Atomic scale nanoengineering

Selective etching of armchair edges in graphene [16]

In 2010 we developed an etching strategy that allowed the parallel production of nanoscale features with zig-zag edges in graphene [Nemes-Incze, P., Magda, G., Kamarás, K. & Biró, L. P. Crystallographically selective nanopatterning of graphene on SiO2. *Nano Res.* **3,** 110–116 (2010)]. We continued our efforts to elaborate a similar procedure for the parallel production of armchair edges, too. We used bulk HOPG in which under conditions of mild oxidation, it was possible on one hand to reveal the location of the grain boundaries, on the other hand, large area hexagonal holes were generated at defect sites. The hexagonal shape of the etched holes shows that the process is crystallographically selective. As we showed by atomic resolution STM images, the edges of the formed holes have armchair orientation, Fig. 10. We also shoved, that it is possible to cleave few layers from the bulk HOPG and transfer them onto SiO_2/Si in such way that the hexagonal holes are preserved.

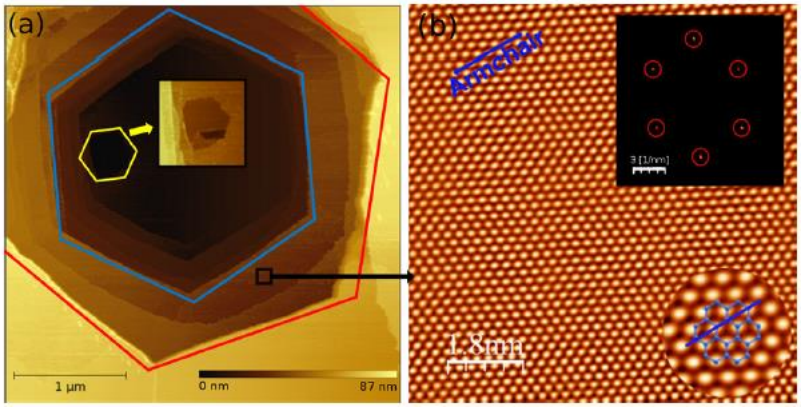

FIG. 10. – (a) STM image of an etched hexagonal hole revealing several graphite grains of different orientation (stacked on top of each other), indicated by the rotated hexagons. Inset: zoomed and lightened image of the yellow mark hole. (b) Atomic resolution STM image near the red hexagonal edge (marked by a black square). Upper inset: Fourier transformed atomic resolution image. The lower inset shows the armchair orientation of the lattice.

Scanning probe microscopy characterization and nanopatterning of CVD graphene [19, 35, 36, 39, 40]

Our results regarding the atomic scale characterization and the nanopatterning of CVD graphene attracted numerous conference invitations and also an invitation to write a review paper on this topic [9].

Armchair and zig-zag edge nanoribbons [26, 34, 38, 41, 42, 53, 54, 55]

From the result related to nanopatterning of CVD graphene the most relevant are those regarding the cutting of nanoribbons with a few nanometers in width and which have a precisely determined crystallographic orientation. This work is based on the procedure (STL) we developed in 2008 for the cutting of such nanoribbons on the surface of bulk HOPG [Tapasztó, L., Dobrik, G., Lambin, P. & Biró, L. P. Tailoring the atomic structure of graphene nanoribbons by scanning tunnelling microscope lithography. *Nat. Nanotechnol.* **3,** 397–401 (2008)]. A major difficulty in the case of CVD graphene was that the Cu surface on which the

graphene is grown starts to oxidize very fast after the first cut in the graphene layer is done by STL. We could solve this difficulty by using stripped gold (Fig. 11), onto which the CVD grown graphene was transferred.

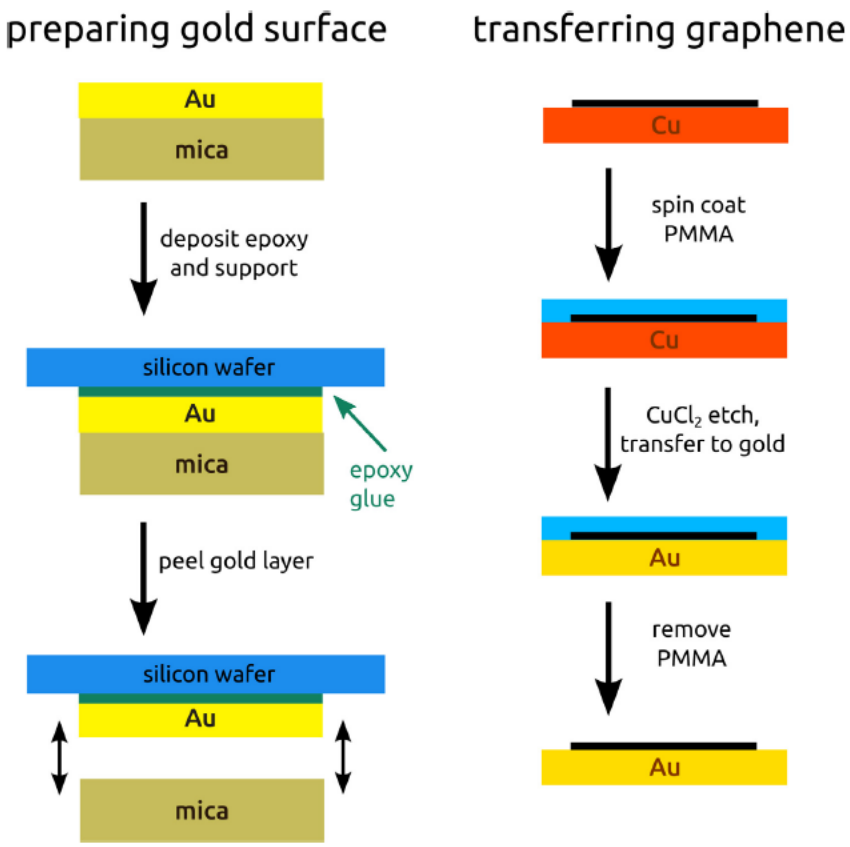

FIG. 11. Preparing the stripped Au surface and transferring the CVD grown graphene onto it.

Once the CVD graphene was on the stripped Au, which "inherited" its atomically smooth surface from the mica layer onto which it was deposited, we could do STL in exactly the same way as we did earlier on the surface of HOPG. We were able for the first time to produce a full range of armchair edged and zig-zag edged nanoribbons of different widths (Fig. 12) and we were able to compare their electronic structure with the theoretical predictions (Fig. 13).

The possibility that non-magnetic materials such as carbon could exhibit a novel type of s–p electron magnetism has attracted much attention over the years, not least because suchmagnetic order is predicted to be stable at high temperatures. We showed that, in contrast to random defect distributions, atomic-scale engineering of graphene edges with specific crystallographic orientation—comprising edge atoms from only one sub-lattice of the bipartite graphene lattice—can give rise to a robust magnetic order. Using STL, a nanofabrication technique we developed based on scanning tunneling microscopy to define graphene nanoribbons with nanometer precision and well-defined crystallographic edge orientations we produced both armachair and zig-zag nanoribbons of a few nanometers in width. The so-called 'armchair' ribbons display quantum confinement gaps in very good agreement with theoretical predictions, ribbons with the 'zigzag' edge structure that are narrower than 7 nanometres exhibit an electronic bandgap of about 0.2–0.3 eV, which can be identified as a signature of interaction-induced spin ordering along their edges. Moreover, upon increasing the ribbon width, a semiconductor-to-metal transition is revealed, indicating the switching of

the magnetic coupling between opposite ribbon edges from the antiferromagnetic to the ferromagnetic configuration. We found that the magnetic order on graphene edges of controlled zigzag orientation can be stable even at room temperature, raising hopes of graphene-based spintronic devices operating under ambient conditions.

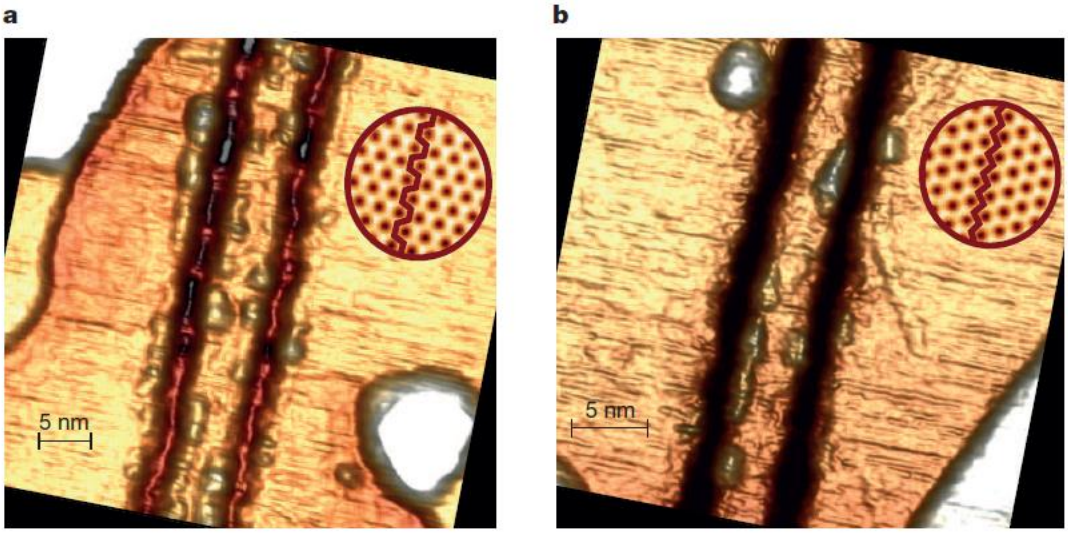

FIG. 12. Graphene nanoribbons with precisely defined crystallographic edge orientations. STM image (500mV, 0.8 nA) of a 5-nmwide graphene nanoribbon with armchair edge orientation (a) and STM image of a 6.5-nm-wide ribbon with edges of precisely zigzag orientation (300 mV, 2 nA) (b) patterned by scanning tunnelling lithography in a graphene sheet deposited on a Au(111) substrate. The circular insets show atomic-resolution STM images, confirming the crystallographic directions of the edges. The atomic-resolution images in the insets were Fourier filtered for clarity. The protrusions on the otherwise highly regular edges are imaging instabilities.

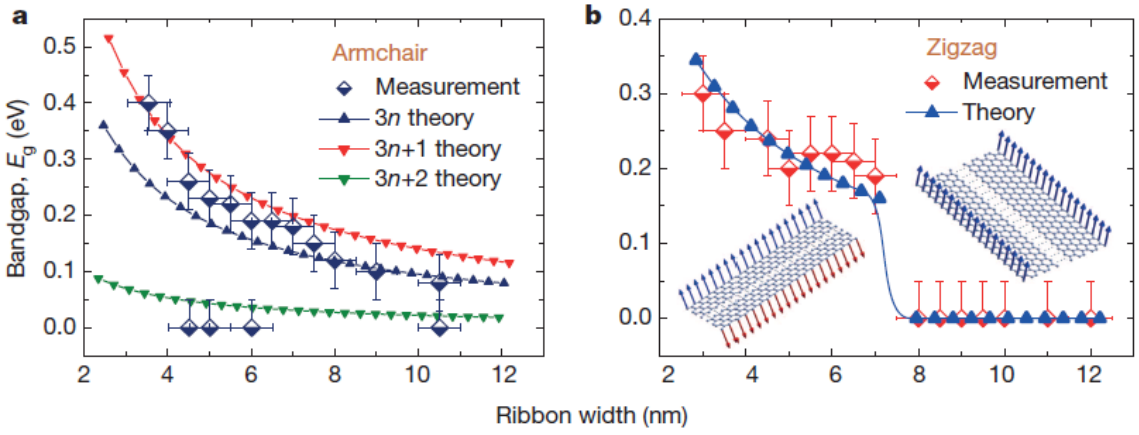

FIG. 13 Edge-specific electronic and magnetic properties of graphene nanoribbons. The bandgap measured by tunneling spectroscopy as a function of ribbon width in armchair (a) and zigzag (b) ribbons. Armchair ribbons display a quantum confinement gap inversely proportional to their width (where n =1, 2, 3,...; is the number of rows of carbon dimers across their width). In zigzag ribbons the band structure is governed by the emerging edge magnetism and a sharp semiconductor (antiferromagnetic) to metal (ferromagnetic) transition is revealed. Theoretical data points were calculated using the mean field Hubbard model (continuous lines are only guides to the eye). Error bars of the measured gap values originate

from thermal broadening and substrate effects; error bars for ribbon widths (horizontal) arise from tip convolution effects.

4. Sub-nanometer rippling of CVD graphene on Cu(111) [6, 23, 24]

We observed for the first time a special growth phenomenon when growing CVD graphene on Cu(111) substrates. During the high temperature phase of the growth a certain fraction of the surface Cu atoms tend to migrate in "pillow-like" structures leaving behind shallow and narrow trenches in the Cu surface, Fig. 14. Both kinds of features are covered by graphene.

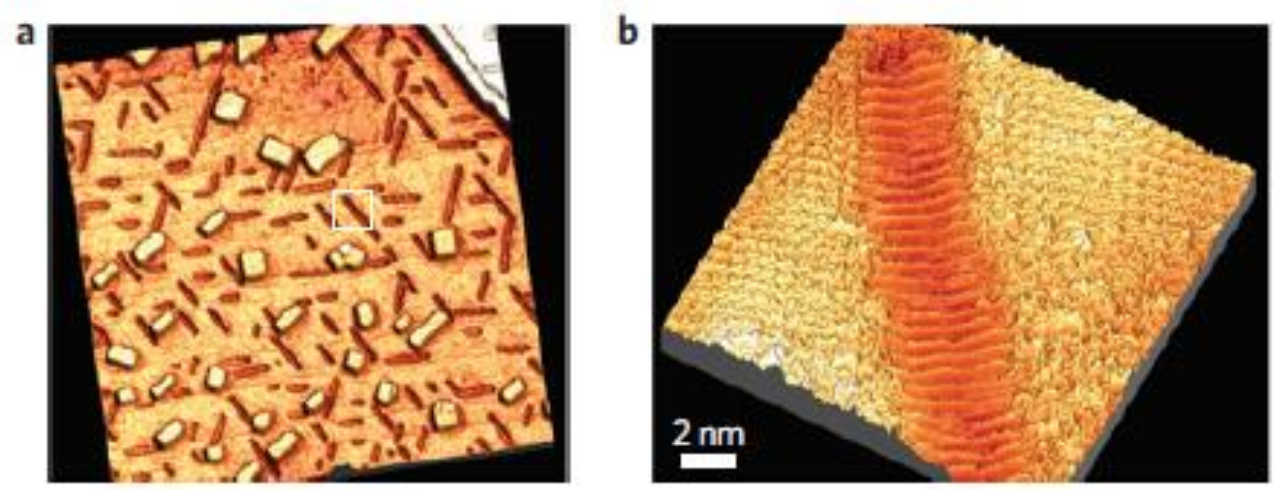

FIG. 14. Three-dimensional STM images of nanotrenches and graphene nanoripples. a) STM image (300 x 300 nm^2) of a reconstructed Cu(111) surface continuously covered by graphene. The rectangular protrusions are single-atom-height Cu adatom clusters, whereas the trench-like features correspond to vacancy islands with well-defined widths of 5nm and oriented along three particular directions. b) High-resolution STM image of a nanotrench revealing the nanoscale periodic rippling of the graphene membrane suspended over the trench.

Understanding how the mechanical behavior of materials deviates at the nanoscale from the macroscopically established concepts is a key challenge of particular importance for graphene, given the complex interplay between its nanoscale morphology and electronic properties. The (sub)nanometre-wavelength periodic rippling of suspended graphene nanomembranes over the trenches produced in the Cu substrate has been realized by thermal strain engineering and investigated using scanning tunneling microscopy. This allowed us to explore the rippling of a crystalline membrane with wavelengths comparable to its lattice constant. The observed nanorippling mode violates the predictions of the continuum model, and evidences the breakdown of the plate idealization of the graphene monolayer. Nevertheless, microscopic simulations based on a quantum mechanical description of the chemical binding accurately describe the observed rippling mode and elucidate the origin of the continuum model breakdown. Spatially resolved tunneling spectroscopy measurements indicate a substantial influence of the nanoripples on the local electronic structure of graphene and reveal the formation of one dimensional electronic superlattices Fig. 15.

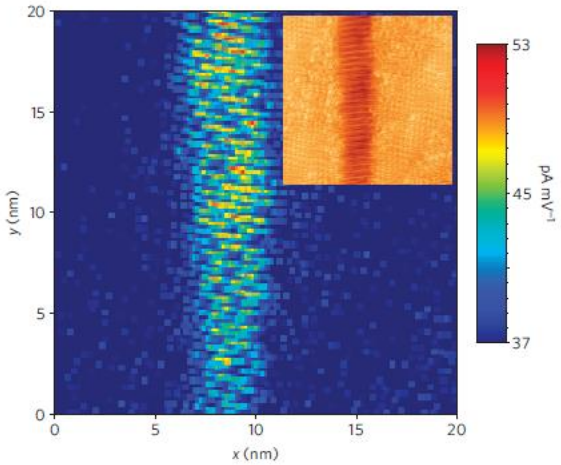

FIG. 15. Local electronic density of states map of graphene nanoripples. Spatially resolved differential tunneling conductivity map (plotted at U_{bias} = 48 mV) exhibiting the periodic modulation of the local density of states on the graphene nanoripples. The inset shows the corresponding topographic image.

5. Vertical wan der Waals heterostructures of 2D materials

Stacking vertically – in a direction normal to the plane of the 2D material – the same 2D material (homostructure) or different 2D materials (heterostructure) opens up a very exciting and broad way for tuning the physical properties of stacks of 2D materials. Not to mention the advantages of encapsulating the active graphene layer between two passivating h-BN layers.

CVD graphene grown on h-BN [10]

In collaboration with our Korean partners we carried out experiments to explore the CVD growth of graphene on h-BN grown by CVD on Cu. We investigated by STM the CVD graphene grown on CVD grown h-BN. First we showed that during the CVD growth of h-BN on polycrystalline Cu, there is a close correlation between the crystallographic orientation of the Cu grains, their coverage by h-BN and compactness of the grown layer (Fig. 16).

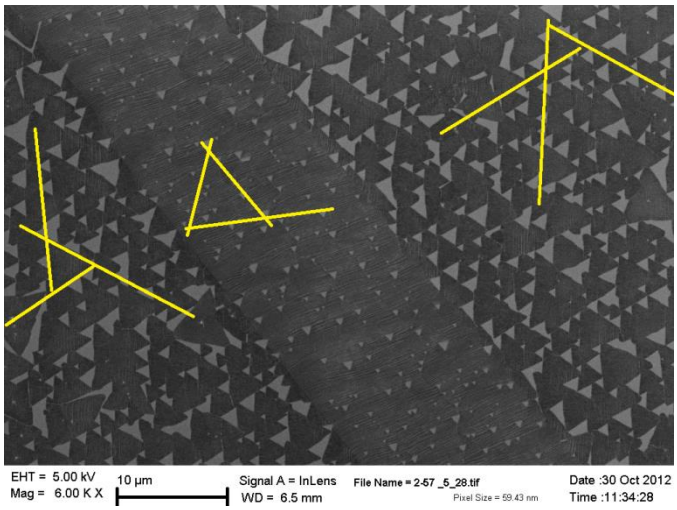

FIG. 16. SEM image of an area with (111)orientation (middle) embedded in area with (100) orientation (left and right sides). The h-BN crystallites are the dark in all the areas. The yellow lines highlight the orientation of the sides of the triangle in the respective area.

Unfortunately, the next step of the CVD growth of graphene on the previously grown h-BN was not successful. The growing graphene layers destroyed the previously grown h-BN. This could be very clearly established by the atomic resolution STM images of the graphene layers, which did not exhibited any sign of moire type images (Fig. 17).

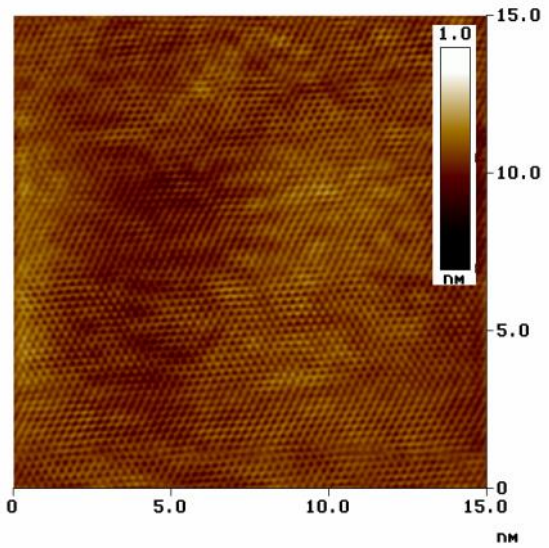

FIG. 17. Typical atomic resolution, topographic STM image acquired on polycrystalline Cu substrate on which h-BN was grown previously.

Graphene on HOPG [49, 66]

A very useful way to investigate the moire type naoarchitectures is to place CVD graphene on HOPG, this can be regarded as a homostructure. In this way we could map the full range of angular misorientations and we revealed several characteristic regions (Fig. 18).

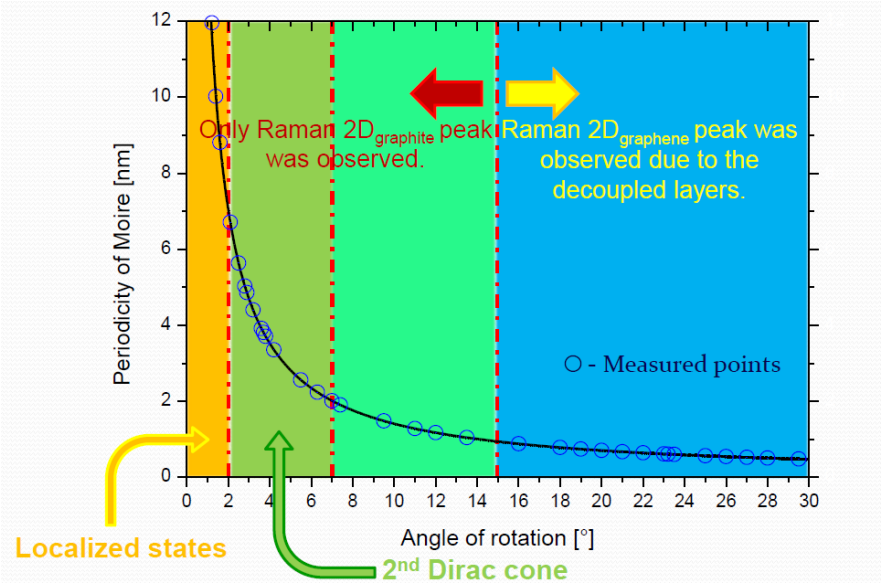

FIG. 18. Summary of the various experimentally realized and investigated nanoarchitectures with angular misorientation from 1.5^{o} to 28^{o} .

When the misorientation angle is below 2^o localizes states could be evidenced by STM measurements and vere confirmed by computer modeling. Between 2^o and 7^o secondary Dirac cones were shown experimentally in the STS spectra. Between 7^o and 15^o the graphene layer and the HOPG substrate are not yet fully decoupled vibrationally. This decoupling becomes complets at misorientation angles exceeding 15^o, as it was shown by Raman spectroscopy.

Exfoliation of other 2D materials [51, 65]

Isolating large-areas of atomically thin transition metal chalcogenide crystals is an important but challenging task. The mechanical exfoliation technique can provide single layers of the highest structural quality, enabling to study their pristine properties and ultimate device performance. However, a major drawback of the technique is the low yield and small (typically < 10 μm) lateral size of the produced single layers. We developed a novel mechanical exfoliation technique, based on chemically enhanced adhesion, yielding MoS_2 single layers with typical lateral sizes of several hundreds of microns (Fig. 19). The idea is to exploit the chemical affinity of the sulfur atoms that can bind more strongly to a gold surface than the neighboring layers of the bulk MoS_2 crystal. Moreover, we found that our exfoliation process is not specific to MoS_2, but can be generally applied for various layered chalcogenides including selenites and tellurides, providing an easy access to large-area 2D crystals for the whole class of layered transition metal chalcogenides.

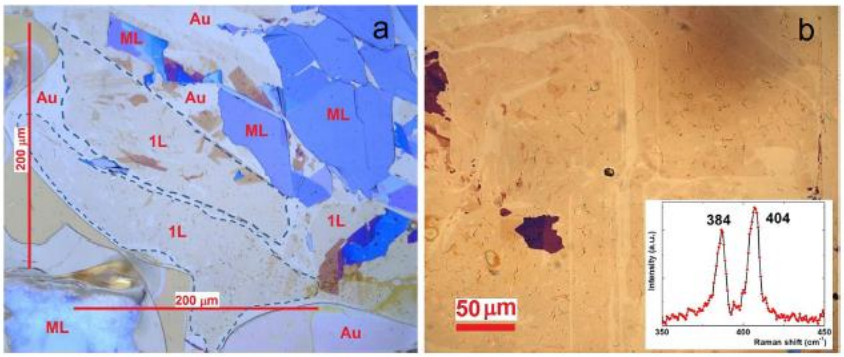

FIG. 19. Mechanical exfoliation through chemically enhanced adhesion of large area MoS_2 single layers. Optical microscopy images (a,b) of MoS_2 single layer areas (1L, outlined by dotted lines) with several hundreds of microns lateral size exfoliated on gold (Au 111) substrate. The flakes of blue color are thick MoS_2 multilayers (ML). The large areas of the faintest optical contrast have been confirmed to be single layers by Raman spectroscopy (inset).

MoS_2 grown on HOPG [58, 59, 60]

Vertically stacked heterostructures of 2D materials are expected to become building blocks of next generation nanoelectronic devices. Therefore, the detailed understanding of their interfaces is of particular importance. In order to gain information on the properties of the graphene-MoS_2 system, we have investigated MoS_2 sheets grown by chemical vapor deposition (CVD) on highly ordered pyrolytic graphite (HOPG) as a model system with atomically clean interface. The results are compared with results reported recently for MoS_2 grown on epitaxial graphene on SiC. Our STM study revealed that the crystallographic orientation of MoS_2 sheets is determined by the orientation of the underlying graphite lattice. This epitaxial orientation preference is so strong that the MoS2 flakes could be moved on

HOPG with the STM tip over large distances without rotation. The electronic properties of the MoS_2 flakes have been investigated using tunneling spectroscopy. A significant modification of the electronic structure has been revealed at flake edges and grain boundaries. These features are expected to have an important influence on the performance of nanoelectronic devices. We have also demonstrated the ability of the STM to define MoS_2 nanoribbons down to 12 nm width, which can be used as building blocks for future nanoelectronic devices.

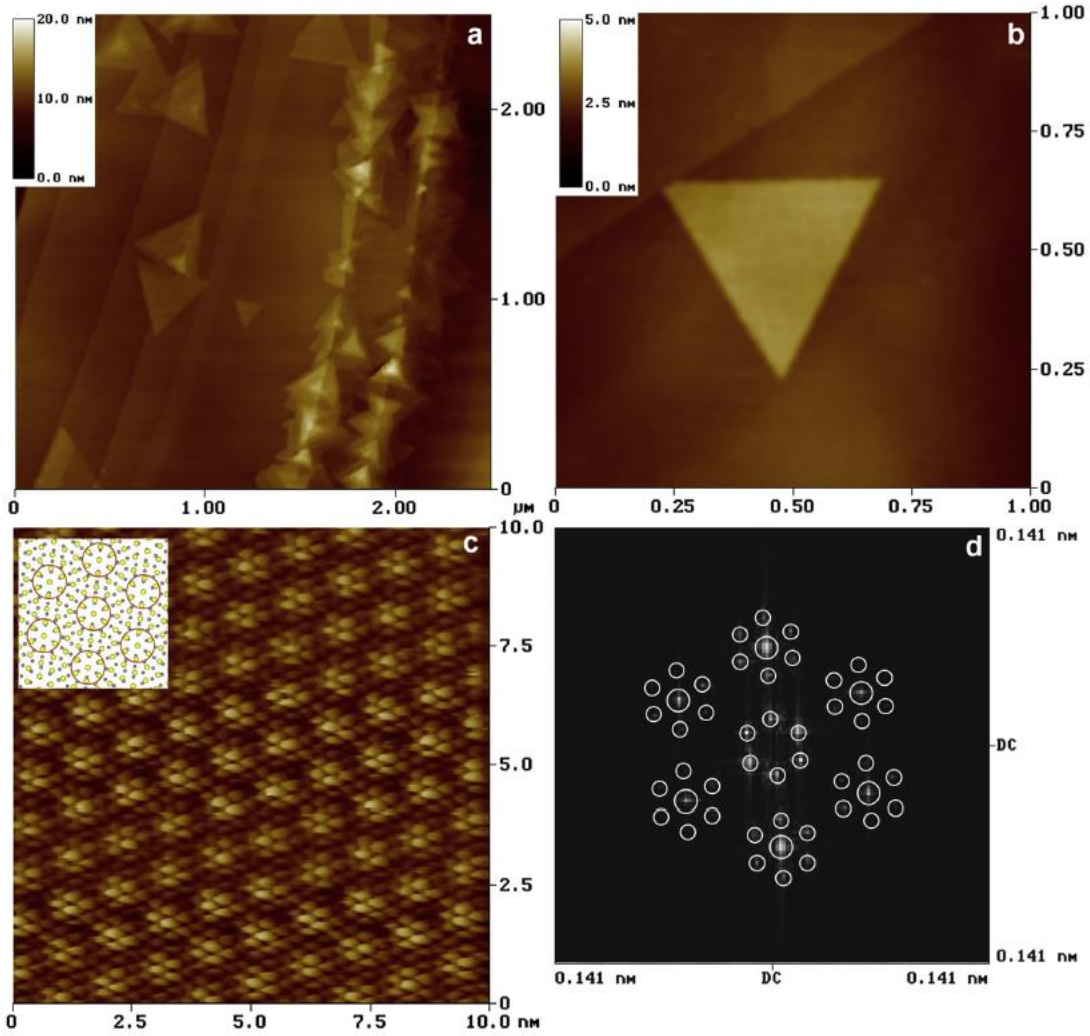

FIG. 20. STM image of MoS_2 flakes grown on HOPG (200 pA, 1.5 V). b) A single layer MoS2 flake. c) Atomic resolution STM image of the flake exhibiting a moire type superlattice (1 nA, 100 mV). The inset shows a schematic model of sulfur (yellow) and carbon (grey) atomic lattices. The red circles denote the overlapping regions. d) FFT of the atomic resolution image with spots highlighted by white circles.

3D heteronanoarchitectures with graphene [32, 33, 46, 47, 48, 56, 57, 61, 62, 63, 68, 69]

Due to its high strength and extreme flexibility graphene can be used to build various 3D heteronanoarchitectures in which one component is constituted by different nanoparticles on bulk substrate, further tuning opportunities are offered by the annealing of the 3D heteronanoarchitecture constituted of graphene and supported nanoparticles. For example, if Au nanoparticles are used, the gold nanoislands can be used to tailor the local electronic properties of graphene. Graphene on crystalline gold nanoislands exhibits moire superlattices,

which generate secondary Dirac points in the local density of states. Conversely, the graphene covered gold regions undergo a polycrystalline / Au (111) phase transition upon annealing. Moreover, the nanoscale coexistence of moire superlattices with different moire periodicities has also been revealed. Several of these moire periodicities are anomalously large, which cannot be explained by the standard lattice mismatch between the graphene and the topmost Au (111) layers. Density functional theory and molecular dynamics simulations show for the first time that in such cases the graphene and the interfacial metallic layer is strained, leading to distorted lattice constants, and consequently to reduced misfit. Room temperature charge localization induced by a large wavelength moire pattern is also observed by scanning tunneling spectroscopy (Fig. 21). These findings can open a route towards the strain engineering of graphene/metal interfaces with various moire superlattices and tailored electronic properties for nanoscale information coding.

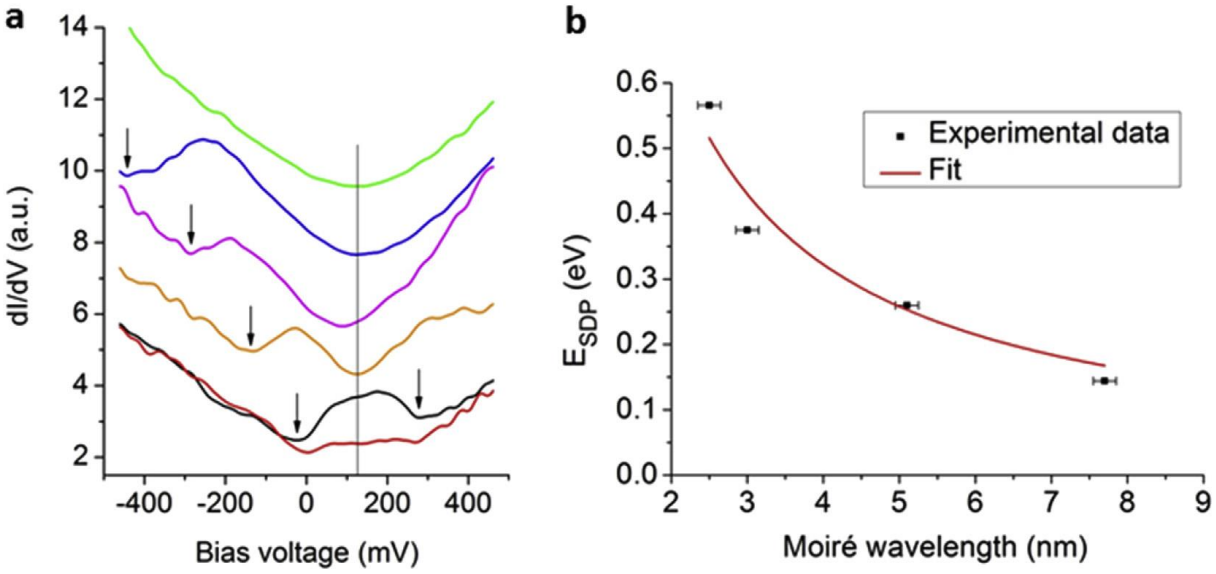

FIG. 21. Local density of states of graphene on Au (111) showing superlattice Dirac points. (a) Experimental dI/dV curves for five different moire wavelengths: 1.9 nm (green), 2.5 nm (blue), 3.0 nm (magenta), 5.1 nm (orange), and 7.7 nm. For this latter, spectra measured on both topographically high (black) and low (red) positions are shown. The vertical line marks the approximate position of the main Dirac point. The secondary dips in the spectra are marked by arrows. Each spectrum is an average of 8 measurements. (b) Energy of the secondary dips measured from the Dirac point, as a function of moire wavelength. The black symbols are experimentally measured values, while the red line is the theoretical fit to the data.

The papers published have a cumulated IF of: 130.079
According to the Web of Science, during the project period these papers received 436 citations (2017.01.23).